PCCP

PAPER

View Article Online
View Journal | View Issue

Cite this: *Phys. Chem. Chem. Phys.*, 2018, **20**, 24940

Unimolecular decomposition kinetics of the stabilised Criegee intermediates CH_2OO and CD_2OO†

Daniel Stone, *[a] Kendrew Au,[b] Samantha Sime,[a] Diogo J. Medeiros,[a]
Mark Blitz,[a] Paul W. Seakins,[a] Zachary Decker‡[b] and Leonid Sheps *[b]

Decomposition kinetics of stabilised CH_2OO and CD_2OO Criegee intermediates have been investigated as a function of temperature (450–650 K) and pressure (2–350 Torr) using flash photolysis coupled with time-resolved cavity-enhanced broadband UV absorption spectroscopy. Decomposition of CD_2OO was observed to be faster than CH_2OO under equivalent conditions. Production of OH radicals following CH_2OO decomposition was also monitored using flash photolysis with laser-induced fluorescence (LIF), with results indicating direct production of OH in the $v = 0$ and $v = 1$ states in low yields. Master equation calculations performed using the Master Equation Solver for Multi-Energy well Reactions (MESMER) enabled fitting of the barriers for the decomposition of CH_2OO and CD_2OO to the experimental data. Parameterisations of the decomposition rate coefficients, calculated by MESMER, are provided for use in atmospheric models and implications of the results are discussed. For CH_2OO, the MESMER fits require an increase in the calculated barrier height from 78.2 kJ mol^{-1} to 81.8 kJ mol^{-1} using a temperature-dependent exponential down model for collisional energy transfer with $\langle \Delta E \rangle_{\text{down}} = 32.6(T/298\ \text{K})^{1.7}$ cm^{-1} in He. The low- and high-pressure limit rate coefficients are $k_{1,0} = 3.2 \times 10^{-4}(T/298)^{-5.81}\exp(-12\,770/T)$ cm^3 s^{-1} and $k_{1,\infty} = 1.4 \times 10^{13}(T/298)^{0.06}\exp(-10\,010/T)$ s^{-1}, with median uncertainty of ~12% over the range of experimental conditions used here. Extrapolation to atmospheric conditions yields $k_1(298\ \text{K}, 760\ \text{Torr}) = 1.1^{+1.5}_{-1.1} \times 10^{-3}$ s^{-1}. For CD_2OO, MESMER calculations result in $\langle \Delta E \rangle_{\text{down}} = 39.6(T/298\ \text{K})^{1.3}$ cm^{-1} in He and a small decrease in the calculated barrier to decomposition from 81.0 kJ mol^{-1} to 80.1 kJ mol^{-1}. The fitted rate coefficients for CD_2OO are $k_{2,0} = 5.2 \times 10^{-5}(T/298)^{-5.28}\exp(-11\,610/T)$ cm^3 s^{-1} and $k_{2,\infty} = 1.2 \times 10^{13}(T/298)^{0.06}\exp(-9800/T)$ s^{-1}, with overall error of ~6% over the present range of temperature and pressure. The extrapolated $k_2(298\ \text{K}, 760\ \text{Torr}) = 5.5^{+9.2}_{-5.5} \times 10^{-3}$ s^{-1}. The master equation calculations for CH_2OO indicate decomposition yields of 63.7% for $H_2 + CO_2$, 36.0% for $H_2O + CO$ and 0.3% for $OH + HCO$ with no significant dependence on temperature between 400 and 1200 K or pressure between 1 and 3000 Torr.

Received 21st August 2018,
Accepted 14th September 2018

DOI: 10.1039/c8cp05332d

rsc.li/pccp

Introduction

Atmospheric oxidation initiated by ozone (O_3) is a key removal mechanism for unsaturated hydrocarbons and volatile organic compounds (VOCs) emitted into the atmosphere, and proceeds *via* the addition of ozone to a carbon–carbon double bond in an ozonolysis reaction.[1,2] Such reactions lead to the production of Criegee intermediates (R_2COO), and are associated with high exothermicities (typically ~250 kJ mol^{-1}).[1] Nascent Criegee intermediates produced in ozonolysis reactions thus contain an excess of internal energy, which can promote unimolecular decomposition, leading to production of key atmospheric species including OH, HO_2 and CO, or can be quenched through collisional energy transfer to surrounding gas molecules, leading to the production of stabilised Criegee intermediates (SCIs) which can undergo further chemistry in the atmosphere.

Recent developments have identified photolytic sources of stabilised Criegee intermediates, facilitating laboratory studies of SCI reaction kinetics.[3,4] Subsequent experimental studies have largely focused on the bimolecular reactions of SCIs, often finding higher reactivity than previously expected, with relatively few studies placing an emphasis on SCI unimolecular decomposition reactions.[5–8] Decomposition reactions of SCIs

---

[a] School of Chemistry, University of Leeds, Leeds, LS2 9JT, UK. E-mail: d.stone@leeds.ac.uk
[b] Combustion Research Facility, Sandia National Laboratories, Livermore, CA 94551, USA. E-mail: lsheps@sandia.gov

† Electronic supplementary information (ESI) available. See DOI: 10.1039/c8cp05332d

‡ Present address: University of Colorado, Boulder, CO 80302, USA.

are potentially important in their own right; furthermore, analysis of SCI decomposition may provide insight to the decomposition of nascent excited CIs produced in atmospheric ozonolysis reactions. In addition, production of the CH_2OO Criegee intermediate in the combustion of the biofuel dimethyl ether (DME, CH_3OCH_3) has been proposed, with unimolecular decomposition of CH_2OO likely to be important under combustion conditions.[9,10] Because CH_2OO decomposition involves possible radical and closed-shell product pathways, the knowledge of its rate coefficient and product branching may explain why no evidence of Criegee intermediates has yet appeared in the combustion studies of DME or larger ethers.

Investigation of the potential energy surface (PES) for CH_2OO decomposition (R1) using quantum chemical calculations at the CCSD(T)/aug-cc-pVTZ//B3LYP/aug-cc-pVTZ level indicated the presence of two main reaction channels that produce formic acid and dioxirane, with barriers of 67.4 and 78.2 kJ mol^{-1}, respectively, and with the formic acid channel proceeding *via* a roaming-like transition state.[11] Both channels potentially lead to the final products $H_2 + CO_2$, $H_2O + CO$, or HCO + OH.

$$CH_2OO \rightarrow H_2 + CO_2 \quad \text{(R1a)}$$

$$\rightarrow H_2O + CO \quad \text{(R1b)}$$

$$\rightarrow HCO + OH \quad \text{(R1c)}$$

However, these calculations apparently underestimated the barrier for the formic acid channel owing to spin-contamination.[12] Higher level multi-reference calculations[12,13] predict a similar barrier of 79.5 kJ mol^{-1} for the dioxirane channel, but a much higher one for the formic acid channel ($\sim$205 kJ mol^{-1}), rendering the formic acid pathway uncompetitive with the dioxirane channel.[12] If active, the formic acid channel would result in a strong kinetic isotope effect between CH_2OO and CD_2OO.

Theoretical studies of the decomposition of vibrationally excited nascent CH_2OO produced in ethene ozonolysis, using high-accuracy calculations performed with HEAT-345(Q), have also revealed potential decomposition pathways involving dioxirane (with a barrier of 79.9 kJ mol^{-1} and ultimately leading to H_2 and CO_2) and formic acid (with final products $H_2 + CO_2$ or $H_2O + CO$). An alternative pathway to that involving dioxirane was also reported, leading to production of OH and HCO, but with a calculated barrier of 133.1 kJ mol^{-1} and thus unlikely to compete with the dioxirane pathway.[14,15]

Experimental evidence for OH production from CH_2OO also comes from studies in which the behaviour of OH radicals has been probed following the photolysis of CH_2I_2 in O_2/Ar gas mixtures.[16,17] These studies have successfully used OH measurements as proxies to determine the kinetics of CH_2OO reactions, including with SO_2. This finding implicates the decomposition of stabilised CH_2OO as the OH radical source, although decomposition kinetics were not directly probed.[16,17] Similarly, a study of SCIs generated by alkene ozonolysis has also identified the decomposition of stabilised CH_2OO as a potential source of OH, but kinetic information was limited and a low OH yield was reported.[18]

Ozonolysis experiments performed in atmospheric simulation chambers have been used to infer the kinetics of stabilised CH_2OO decomposition, but with large uncertainties, since first-order losses of CH_2OO by physical processes such as wall reactions are difficult to distinguish from loss through unimolecular decomposition. A recent series of chamber experiments at atmospheric temperature and pressure reported an upper limit of 4.2 s^{-1} for the first-order loss of stabilised CH_2OO, which includes a contribution from the decomposition reaction.[19,20] This value was determined by measuring the ratio of the rate coefficient for first-order losses to that for the reaction of CH_2OO with SO_2, and the decomposition rate was indistinguishable from zero within the measurement uncertainties.[19,20]

Measurements of photolytically generated CH_2OO using cavity ringdown spectroscopy (CRDS) have also been used to infer the unimolecular decomposition kinetics in N_2 at 293 K in the pressure range 7 to 30 Torr, giving an upper limit to the decomposition rate coefficient of (11.6 ± 8.0) s^{-1}. Similarly to the results obtained in the chamber experiments, the first-order removal of CH_2OO in the CRDS measurements contains not only the contribution from the unimolecular decomposition but also contributions from physical processes such as diffusion and wall loss.[21] A similar upper limit to the rate coefficient for decomposition of (9.4 ± 1.7) s^{-1} was reported from an investigation of the reactions of CH_2OO with SO_2 and water vapour at 293 K and atmospheric pressure.[22]

A further investigation of the decomposition of stabilised CH_2OO was performed using a free-jet flow reactor, in which CH_2OO was produced by ozonolysis of ethene in air and monitored by sampling from the flow reactor and titration to H_2SO_4 through reaction with SO_2.[23] The design of the free-jet flow reactor reduces wall losses, and the pressure used in the reactor inhibits losses through diffusion, thus minimising the contributions to CH_2OO loss from physical processes. The study reported a rate coefficient for stabilised CH_2OO decomposition of (0.19 ± 0.07) s^{-1} at 297 K and 1 bar, with quantum chemical calculations at the CCSD(T)/aug-cc-pVTZ level giving a calculated barrier height to decomposition of 78.9 kJ mol^{-1}.[23] A high pressure limiting rate coefficient of 0.25 s^{-1} was determined from master equation calculations at 297 K,[23] similar to that obtained in an earlier theoretical study,[24] with fall-off behaviour predicted at the pressure of the experiment and predictions for the rate coefficient at 1 bar between 0.037 s^{-1} and 0.12 s^{-1}.[23] Improved agreement with the experimental value was achieved by a reduction in the calculated barrier height to 76.8 kJ mol^{-1}, resulting in an increase in the predicted high pressure limiting rate coefficient to 0.58 s^{-1} at 297 K and predictions for the rate coefficient at 1 bar and 297 K between 0.08 s^{-1} and 0.26 s^{-1}.[23]

Thus, while there have been several attempts to determine the decomposition kinetics of stabilised CH_2OO Criegee intermediates, the results have large uncertainties, and the most reliable measurements obtained using the free-jet flow reactor have only been reported at a single temperature and pressure. Full assessment of the impacts of stabilised CH_2OO decomposition in the atmosphere, where it may be in competition with $CH_2OO + SO_2$ at low SO_2 concentrations given the range of CH_2OO decomposition rate coefficients reported in the literature (0.037–$11.6\ s^{-1}$), and in chamber studies of ozonolysis reactions, is therefore hindered by a lack of measurements of stabilised CH_2OO kinetics over a wide range of temperatures and pressures. In this work we report a detailed study of the decomposition kinetics of stabilised CH_2OO (k_1) and CD_2OO (k_2) as a function of temperature and pressure.

$$CH_2OO \rightarrow \text{products} \qquad \text{(R1)}$$

$$CD_2OO \rightarrow \text{products} \qquad \text{(R2)}$$

Flash photolysis of $CH_2I_2/O_2/He$ and $CD_2I_2/O_2/He$ gas mixtures coupled with time-resolved cavity enhanced broadband UV absorption spectroscopy was used to monitor changes in CH_2I_2/CD_2I_2, CH_2OO/CD_2OO and IO to determine the kinetics at pressures between 2 and 350 Torr and temperatures between 450 and 650 K, thereby increasing the decomposition rate and minimising effects of physical losses of SCI. The production of OH radicals from CH_2OO decomposition was also investigated using flash photolysis of $CH_2I_2/O_2/N_2$ coupled with laser-induced fluorescence (LIF) spectroscopy at temperatures between 500 and 600 K and pressures in the range 10 to 95 Torr. We discuss the results from the UV experiments in which CH_2OO and CD_2OO are directly monitored, and compare the results to probe any potential kinetic isotope effects in the decomposition mechanism. We then discuss the LIF experiments in which the OH products from stabilised CH_2OO are probed, and compare the results to the UV experiments. Finally, we discuss the results from Master equation calculations, using the Master Equation Solver for Multi-Energy well Reactions (MESMER),[25] which were performed to fit the barrier height for CH_2OO decomposition to the CH_2OO decomposition kinetics determined in the UV experiments, thus providing a theoretical framework for the reaction and a full parameterisation as a function of temperature and pressure.

Experimental

UV absorption

Time-resolved cavity-enhanced broadband UV absorption spectroscopy experiments were performed at the Sandia National Laboratories, Livermore, USA, using experimental apparatus described in detail in previous publications.[26–28] Precursor gas mixtures containing CH_2I_2 (or CD_2I_2), entrained in He, O_2, and He buffer gas were admitted into a quartz flow cell using calibrated mass flow controllers (MKS Instruments). Chemistry in the reaction cell was initiated by the photolysis of the di-iodo precursor at a wavelength of 266 nm, which was generated by the 4th harmonic of an Nd:YAG laser (Continuum Surelite III) with a typical fluence of $\sim 19\ mJ\ cm^{-2}$, with O_2 concentrations such that the production of CH_2OO (or CD_2OO) was rapid compared to the subsequent decay. Transient absorptions in the reaction cell were monitored using a Xe arc lamp (Newport Corp.), which was reflected between two concave high reflectivity mirrors (JDSU Inc.) forming an optical resonator cavity 1.6 m in length, operating over probe wavelengths between 300 and 450 nm simultaneously with total effective absorption path length of 40–56 m. Light exiting the optical cavity was directed into a time-resolved spectrometer, consisting of a rotating mirror, synchronized with the photolysis laser, that rapidly sweeps the probe beam vertically, followed by a ruled grating, which provides spectral dispersion in the horizontal plane. Spectral and temporal information contained in the probe beam are thus spatially mapped onto the horizontal and vertical position, respectively, at the focal plane of the spectrometer. The time evolution of the entire broadband cavity output is recorded by a TEC-cooled 1024 × 1024-element CCD camera for every laser shot, and averaged on-chip (300–600 shots in the present work), prior to transfer to a computer for data analysis.

Transient absorption spectra were computed by Beer's Law from the difference between probe light intensities with (I_{ON}) and without (I_{OFF}) the photolysis laser: $OD(\lambda,t) = -\ln(I_{ON}(\lambda,t)/I_{OFF}(\lambda,t))$. The mirror rotation was adjusted between 1 and 10 Hz (corresponding to total observation times between 13.5 and 1.35 ms, respectively) as needed to capture the kinetics under investigation. The experimental resolution of this spectrometer is ultimately determined by spatial focusing of the probe beam on the CCD sensor: ∼7 pixels (FWHM), corresponding to spectral resolution of ∼1.5 nm and temporal resolution of ∼9–90 μs, depending on the mirror rotation frequency. The total flow rate through the reaction cell was adjusted with changes in pressure and laser repetition rate to ensure a fresh sample of gas in the cell for each photolysis shot.

The pressure in the reaction cell was maintained by a roots pump and actively controlled by a butterfly valve throttling the exit of the cell. Temperatures in the reaction cell were controlled by a series of ceramic heaters (Watlow) surrounding the cell and monitored by K-type thermocouples situated along the length of the reaction cell. Experiments were performed in He (Matheson, 99.9999%) at pressures between 2 and 350 Torr and at temperatures in the range 450 to 650 K, with CH_2I_2 (Aldrich, 99%)/CD_2I_2 (Aldrich, 98%) concentrations in the range 8×10^{12} to $8 \times 10^{13}\ cm^{-3}$ and O_2 (Matheson, 99.9999%) concentrations varied between 1×10^{16} and $7 \times 10^{18}\ cm^{-3}$. Gases and chemicals were used as supplied.

Concentrations of CH_2OO were determined by fitting reference spectra for the CH_2I_2 precursor, CH_2OO and IO (generated by secondary chemistry within the system) to the observed total absorbance between 300 and 440 nm for each time point throughout the reaction. Typical absorbance signals of 10^{-3}–10^{-4} were measured in this work, which correspond to changes in concentration of 0.001–0.0001% (assuming 100% photodissociation on absorption of a photon), which is insignificant compared to the changes in concentration owing to reaction. Fig. 1 shows a typical concentration–time profile for CH_2OO. Details regarding the fitting procedure are given in the ESI.†

Laser-induced fluorescence

Laser-induced fluorescence (LIF) experiments were performed at the University of Leeds, UK, in a slow flow reactor which has been described in detail in previous work.[29–31] Precursor gas

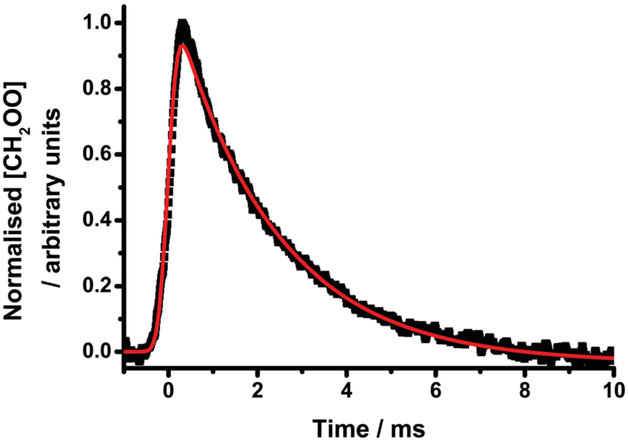

Fig. 1 Normalised concentrations of CH_2OO following photolysis of $CH_2I_2/O_2/He$ at a temperature of 525 K and pressure of 5 Torr (black points) and the result of a first-order kinetic fit to the data (red line), convoluted with a Gaussian instrument function, giving a decay rate coefficient $k_{1,obs}$ = (440 ± 10) s^{-1}. The fit residuals are discussed in further detail in the ESI.†

mixtures ($CH_2I_2/O_2/N_2$) were prepared in a glass gas manifold and passed into a stainless steel six-way cross at known flow rates determined by calibrated mass flow controllers (MKS Instruments). Photolysis of CH_2I_2, leading to rapid production of CH_2OO, was achieved at a wavelength of 355 nm using the 3rd harmonic of an Nd:YAG laser (Continuum Powerlite 8010). Experiments were typically performed at a repetition rate of 10 Hz, although the lasers were also operated at lower repetition rates to ensure that there were no interferences from photolysis products. The laser fluence was typically ~20 mJ cm^{-2}.

The pressure in the reaction cell was monitored by a capacitance manometer, and was maintained by a rotary pump throttled by a needle valve on the exhaust line. Heating of the reaction cell was achieved by a series of cartridge heaters surrounding the cell, with temperatures monitored by K-type thermocouples situated close to the reaction zone.

OH radicals produced in the system were monitored by off-resonance laser-induced fluorescence following either $A^2\Sigma(v' = 1) \leftarrow X^2\Pi(v'' = 0)$ excitation at a wavelength of 282 nm for detection of OH in the ground vibrational state, $OH(v'' = 0)$, or $A^2\Sigma(v' = 1) \leftarrow X^2\Pi(v'' = 1)$ excitation at 288 nm for detection of OH in its first vibrationally excited state, $OH(v'' = 1)$. The 532 nm output of a Nd:YAG laser (Continuum Powerlite 8010) was used to pump a dye laser (Spectra Physics PDL-3) operating on either Rhodamine-6-G or pyromethene 597 dye, with the dye output frequency-doubled to generate light at 282 or 288 nm, respectively. For both excitation wavelengths, the off-resonant OH fluorescence at ~308 nm was passed through an interference filter (Barr Associates, (308 ± 5) nm) and monitored by a channel photomultiplier (CPM, Perkin-Elmer C1943P) mounted perpendicular to the plane of photolysis and probe laser beams. The CPM signal was digitised and integrated on an oscilloscope (LeCroy LT262) prior to being passed to a computer for data analysis. The time delay between the photolysis and probe laser pulses was controlled by a digital delay generator (SRS DG535) and varied to enable monitoring of the OH profiles as a function of time following photolysis of the gas mixture. Kinetic traces typically consisted of 200 time points, with each time point averaged 5–10 times.

Experiments were performed in N_2 (BOC, oxygen free, 99.99%) at pressures between 10 and 95 Torr and at temperatures in the range 480 to 570 K, with CH_2I_2 (Sigma-Aldrich, 99%) concentrations in the range 4×10^{12} to 2×10^{15} cm^{-3} and O_2 (BOC, 99.999%) concentrations varied between 3.7×10^{16} and 5.8×10^{17} cm^{-3}. Gases and chemicals were used as supplied.

Results

UV absorption

CH_2OO. Fig. 1 shows a typical concentration–time profile for CH_2OO determined from the observed absorbance between 300 and 440 nm. The CH_2OO profiles were fitted to a first-order loss process, convolved with a Gaussian instrument response function, which was determined by the spatial profile of the incident probe light on the CCD detector.[26] Fits to a mixed first- and second-order loss process were also examined, but were insensitive to any second-order loss and gave first-order losses within 5% of those obtained from the fits considering first-order loss only. The results obtained from the first-order fits are shown in Fig. 2 as a function of temperature and pressure, and are given in Table 1. Experiments in which the pulse repetition rate of the photolysis laser was varied did not yield any significant differences in the fitted rate coefficients describing the CH_2OO decays.

At temperatures below 500 K, there is little variation in the observed rate coefficients as a function of pressure, although there is an increase from 450 K to 475 K. At temperatures of 500 K and above, the rate coefficients increase with increasing temperature and pressure. The loss of CH_2OO thus appears to contain contributions from two processes, a pressure- and temperature-dependent term, $k(p,T)$, and a pressure-independent temperature-dependent term, $k(T)$. Given the PES for CH_2OO decomposition,[11,12,14,23] we attribute the pressure-dependent term to CH_2OO decomposition, and the pressure-independent term to other background losses of CH_2OO, such that the observed rate coefficient, $k_{1,obs}$, is given by the sum of $k_1(p,T)$ and $k_{1,bg}(T)$. A global fit using data at all temperatures and pressures was performed to determine $k_1(p,T)$ and $k_{1,bg}(T)$, with $k_1(p,T)$ described by the basic Troe equation[32] as shown in eqn (1):

$$k_{1,\mathrm{obs}}(p,T) = \left(\frac{k_{1,0}(T)[\mathrm{M}]}{1+\left(\frac{k_{1,0}(T)[\mathrm{M}]}{k_{1,\infty}(T)}\right)}\right) \times F_{\mathrm{c}}^{\left\{1+\left[\log_{10}\left(\frac{k_{1,0}(T)[\mathrm{M}]}{k_{1,\infty}(T)}\right)\right]^2\right\}^{-1}} + k_{1,\mathrm{bg}}(T) \quad (1)$$

where $k_{1,0}(T)$ is the low-pressure limiting rate coefficient for CH_2OO decomposition, $k_{1,\infty}(T)$ is the high-pressure limiting rate coefficient for CH_2OO decomposition, M is the total number density, F_c is the broadening factor, and $k_{1,bg}(T)$ is

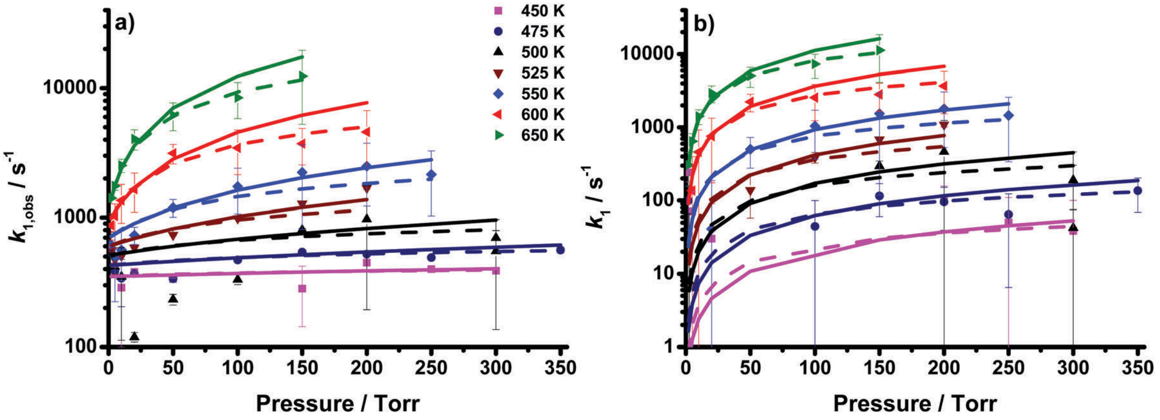

Fig. 2 Rate coefficients describing (a) the observed decay of CH_2OO ($k_{1,obs}$) and (b) the decomposition of CH_2OO ($k_1 = k_{1,obs} - k_{1,bg}$) as a function of temperature and pressure (coloured points) determined from the UV experiments. Fits to the Troe equation (dashed lines) and MESMER simulations using optimised barrier heights and $\langle \Delta E \rangle_{down}$ (solid lines) are also shown. Error bars are 1σ.

the pressure-independent rate coefficient for secondary background removal processes for CH_2OO.

Fits to eqn (1) were performed with $k_{1,bg}(T)$ either constrained to Arrhenius behaviour or unconstrained, *i.e.* allowed to float independently at each temperature. The fits with $k_{1,bg}(T)$ constrained to Arrhenius behaviour gave a lower χ^2 value, although the parameterisations from each fit were in agreement within the fit uncertainties. The fit with $k_{1,bg}(T)$ constrained to Arrhenius behaviour gives $k_{1,0} = (1.3 \pm 4.1) \times 10^{-8}\exp(-(9130 \pm 2080)/T)$ cm^3 s^{-1} and $k_{1,\infty} = (2.4 \pm 9.8) \times 10^{10}\exp(-(8460 \pm 2660)/T)$ s^{-1}, with F_c fixed to a value of 0.6,[33,34] and $k_{bg} = (1.5 \pm 1.1) \times 10^4\exp(-(1680 \pm 400)/T)$ s^{-1}. While the uncertainties in the individual Arrhenius parameters describing $k_{1,0}(T)$, $k_{1,\infty}(T)$ and $k_{1,bg}$ are large, inspection of the covariance matrix (given in the ESI†) indicates that the fit parameters are highly correlated. A complete uncertainty analysis (described in the ESI†), incorporating the correlations between the fit parameters shows that the overall uncertainty in the fit ranges from 3% at the highest temperatures and pressures to 17% at the lowest temperatures and pressures, with a median of 10%. The full results are given in Table 1. While this parameterisation can be used to provide a value for k_1 at 298 K and 760 Torr, the extrapolation is subject to significant uncertainties since the experiments do not cover a sufficiently broad range of pressures in the fall-off regime. Instead, the parameterisation is performed primarily to determine the contributions to the total loss from decomposition and background losses, with the pressure and temperature dependence of the decomposition best described by the Master Equation treatment discussed below.

The pressure-independent background losses of CH_2OO, $k_{1,bg}(T)$, demonstrate the presence of removal processes other than CH_2OO decomposition, including wall losses and secondary chemical loss of CH_2OO. Given the magnitude and temperature dependence of the pressure-independent contribution to the loss, chemical reactions of CH_2OO are likely to be the dominant factor. Results from mixed-order fits to the observed decays indicated little sensitivity to second-order processes, and thus a negligible contribution from CH_2OO self-reaction. At 450 K, the data suggest a contribution from reaction between CH_2OO and CH_2I_2 (see ESI†), with a bimolecular rate coefficient of $(8.2 \pm 1.7) \times 10^{-12}$ cm^3 s^{-1}. The reaction has also recently been observed by Liu *et al.*,[17] with a rate coefficient of $(5.2 \pm 2.6) \times 10^{-14}$ cm^3 s^{-1} at 298 K. At temperatures above 450 K, concentrations of CH_2I_2 were not varied over a sufficient range to fully assess the role of CH_2OO + CH_2I_2; however, the results overall are consistent with the pressure-independent loss term at all temperatures coming largely from the pseudo-first-order loss of CH_2OO through reaction with CH_2I_2.

CD_2OO. Experiments were also performed in which CD_2I_2 was photolysed in the presence of excess O_2 to generate CD_2OO at temperatures between 450 and 650 K. Fig. 3 shows the normalised absorption spectra for CH_2OO and CD_2OO determined from experiments reported in this work at 295 K and 10 Torr (see ESI† for details regarding characterisation of the spectra and fitting to determine normalised concentrations). The spectra are broadly similar in both shape and the position of the peak absorption cross-section, in agreement with a recent report of the CD_2OO spectrum.[35] While previous studies of the CH_2OO[26,36,37] and CD_2OO[35] spectra have shown the presence of vibronic structure at wavelengths above 340 nm, the resolution of the experiments reported here was insufficient to resolve the vibronic structure for either CH_2OO or CD_2OO.

Decays for CD_2OO were fit to first-order loss kinetics, convolved with a Gaussian instrument function, and the observed rate coefficients are shown in Fig. 4 and Table 2. Similarly to CH_2OO, the rate coefficients describing the decays of CD_2OO exhibit pressure dependence at temperatures of 500 K and above, but not at 450 K, indicating contributions from both the pressure-dependent CD_2OO decomposition (k_2) and pressure-independent secondary background losses ($k_{2,bg}$). The observed rate coefficients for the CD_2OO decays were thus fit to an analogous expression to eqn (1) given for CH_2OO. We propose that the background loss of CD_2OO is, at least in part, a result of reaction with CD_2I_2. However, constraining $k_{2,bg}(T)$ to Arrhenius behaviour gave poor fits to data at 450 K, where the background loss dominates

Table 1 Decomposition kinetics of CH_2OO determined from the UV experiments. $k_{1,\mathrm{obs}}$ are the fitted CH_2OO decay rate coefficients, with 1σ listed errors. Fits to $k_{1,\mathrm{obs}}$ are derived using eqn (1), with listed errors given by the uncertainty analysis incorporating correlations between fit parameters as described in the ESI. $k_{1,\mathrm{Troe}}$ and $k_{1,\mathrm{bg}}$ are as defined in eqn (1). $k_{1,\mathrm{MESMER}}$ are the results of MESMER calculations. Data shown in italics were not included in the MESMER fits owing to the observed loss being dominated by the background losses. The uncertainties in $k_{1,\mathrm{MESMER}}$ are estimated from the combined uncertainties in $k_{1,\mathrm{obs}}$ and the Troe fits to $k_{1,\mathrm{obs}}$. High pressure limiting rate coefficients ($p = \infty$) are estimated from MESMER simulations up to p = 10 atm

T/K	p/Torr	$k_{1,\mathrm{obs}}/\mathrm{s}^{-1}$	Fit to $k_{1,\mathrm{obs}}/\mathrm{s}^{-1}$	$k_{1,\mathrm{Troe}}/\mathrm{s}^{-1}$	$k_{1,\mathrm{bg}}/\mathrm{s}^{-1}$	$k_{1,\mathrm{MESMER}}/\mathrm{s}^{-1}$
450	*2*	*590 ± 9*	*351 ± 60*	*1*	*350*	*0.5 ± 0.1*
	5	*420 ± 7*	*352 ± 60*	*2*	*350*	*1.2 ± 0.2*
	10	*290 ± 190*	*354 ± 60*	*4*	*350*	*2.4 ± 0.4*
	20	*380 ± 6*	*357 ± 59*	*7*	*350*	*5 ± 1*
	50	*330 ± 6*	*365 ± 59*	*15*	*350*	*11 ± 2*
	150	*280 ± 140*	*381 ± 58*	*31*	*350*	*29 ± 5*
	200	*450 ± 10*	*386 ± 58*	*36*	*350*	*38 ± 7*
	250	*400 ± 11*	*391 ± 59*	*41*	*350*	*46 ± 9*
	300	*390 ± 18*	*395 ± 59*	*45*	*350*	*53 ± 10*
	∞					*2800 ± 2600*
475	*2*	*530 ± 13*	*428 ± 58*	*2*	*426*	*2 ± 0*
	5	*390 ± 11*	*431 ± 57*	*5*	*426*	*4 ± 1*
	10	*340 ± 130*	*436 ± 57*	*10*	*426*	*7 ± 1*
	20	*370 ± 9*	*445 ± 57*	*19*	*426*	*14 ± 2*
	50	*340 ± 8*	*466 ± 56*	*40*	*426*	*34 ± 5*
	100	*470 ± 10*	*491 ± 54*	*65*	*426*	*63 ± 9*
	150	*540 ± 10*	*510 ± 54*	*84*	*426*	*90 ± 14*
	200	*520 ± 10*	*524 ± 55*	*98*	*426*	*116 ± 19*
	250	*490 ± 20*	*537 ± 56*	*111*	*426*	*141 ± 23*
	350	*560 ± 30*	*558 ± 61*	*132*	*426*	*188 ± 33*
	∞					*9200 ± 8400*
500	*3*	*520 ± 20*	*516 ± 55*	*8*	*508*	*6 ± 1*
	5	*420 ± 10*	*521 ± 54*	*13*	*508*	*10 ± 1*
	10	*350 ± 240*	*534 ± 54*	*26*	*508*	*20 ± 2*
	20	*120 ± 10*	*555 ± 56*	*47*	*508*	*39 ± 4*
	50	*230 ± 20*	*608 ± 59*	*100*	*508*	*91 ± 10*
	100	*330 ± 30*	*669 ± 52*	*161*	*508*	*171 ± 21*
	150	*800 ± 20*	*714 ± 49*	206	508	*246 ± 32*
	200	*970 ± 780*	*750 ± 54*	242	508	*317 ± 44*
	300	*550 ± 410*	*807 ± 62*	299	508	*449 ± 66*
	300	*700 ± 100*	*807 ± 62*	299	508	*449 ± 66*
	∞					*27 000 ± 25 000*
525	*3*	*560 ± 10*	*613 ± 56*	*16*	*597*	*13 ± 2*
	5	*470 ± 110*	*628 ± 54*	*31*	*597*	*25 ± 3*
	10	*510 ± 10*	*655 ± 55*	*58*	*597*	*48 ± 4*
	20	*590 ± 10*	*705 ± 66*	*108*	*597*	*94 ± 8*
	50	740 ± 10	823 ± 80	226	597	222 ± 21
	100	990 ± 10	961 ± 63	364	597	418 ± 44
	150	1280 ± 20	1062 ± 55	465	597	601 ± 67
	200	1690 ± 30	1143 ± 68	546	597	773 ± 90
	∞					70 000 ± 64 000
550	*2*	*620 ± 20*	*717 ± 63*	*27*	*690*	*23 ± 3*
	5	*500 ± 270*	*754 ± 60*	*64*	*690*	*55 ± 5*
	10	*560 ± 230*	*812 ± 68*	*122*	*690*	*107 ± 8*
	20	730 ± 110	916 ± 95	226	690	209 ± 15
	50	1190 ± 190	1163 ± 128	473	690	493 ± 38
	100	1740 ± 670	1453 ± 98	763	690	929 ± 80
	150	2230 ± 1420	1664 ± 80	974	690	1336 ± 123
	200	2490 ± 1260	1832 ± 101	1142	690	1722 ± 167
	250	2150 ± 1120	1975 ± 131	1285	690	2092 ± 212
	∞					170 000 ± 160 000
600	*2*	*870 ± 200*	*988 ± 97*	*97*	*891*	*87 ± 9*
	5	1030 ± 240	1125 ± 93	234	891	213 ± 15
	10	1350 ± 450	1336 ± 121	445	891	417 ± 25
	20	1650 ± 550	1714 ± 190	823	891	812 ± 45
	50	3130 ± 540	2613 ± 270	1722	891	1926 ± 108
	100	3450 ± 1300	3664 ± 210	2773	891	3641 ± 218
	150	3720 ± 1170	4427 ± 157	3536	891	5246 ± 333
	200	4580 ± 2140	5037 ± 178	4146	891	6774 ± 451
	∞					770 000 ± 720 000

Table 1 (*continued*)

T/K	p/Torr	$k_{1,\mathrm{obs}}/\mathrm{s}^{-1}$	Fit to $k_{1,\mathrm{obs}}/\mathrm{s}^{-1}$	$k_{1,\mathrm{Troe}}/\mathrm{s}^{-1}$	$k_{1,\mathrm{bg}}/\mathrm{s}^{-1}$	$k_{1,\mathrm{MESMER}}/\mathrm{s}^{-1}$
650	2	1410 ± 10	1424 ± 150	318	1106	289 ± 29
	5	1750 ± 130	1801 ± 123	695	1106	646 ± 50
	10	2530 ± 300	2429 ± 133	1323	1106	1268 ± 85
	20	4050 ± 730	3552 ± 213	2446	1106	2473 ± 151
	50	6190 ± 1500	6221 ± 322	5115	1106	5879 ± 335
	100	8440 ± 2620	9338 ± 288	8232	1106	11 149 ± 615
	150	12 400 ± 7140	11 599 ± 305	10 493	1106	16 103 ± 875
	∞					2 800 000 ± 2 600 000

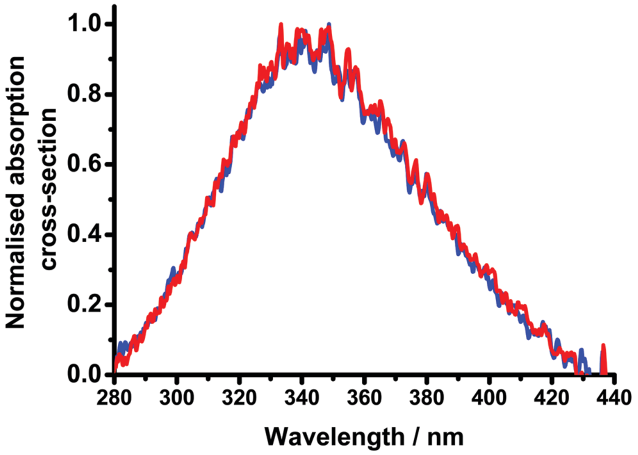

Fig. 3 Normalised absorption spectra for CH_2OO (blue) and CD_2OO (red) determined in this work at 295 K and 10 Torr. Details regarding the characterisation of the spectra are given in the ESI.†

the observed decay, potentially owing to fewer data points compared to CH_2OO. The fits with $k_{2,\mathrm{bg}}$ unconstrained to Arrhenius behaviour give $k_{2,0} = (1.5 \pm 4.0) \times 10^{-11}\exp(-(4640 \pm 1800)/T)$ cm^3 s^{-1} and $k_{2,\infty} = (6.4 \pm 86.7) \times 10^{15}\exp(-(14\,750 \pm 7800)/T)$ s^{-1} with F_c fixed at a value of 0.6. Values for $k_{2,\mathrm{bg}}$ are summarised in Table 2 and can be approximated by the expression $k_{2,\mathrm{bg}} = (2.4 \pm 6.9) \times 10^4\exp(-(2080 \pm 1570)/T)$ s^{-1}. Similarly to the parameterisation for CH_2OO decomposition, the uncertainties in the individual fit parameters for $k_{2,\mathrm{obs}}$ are deceptively large, owing to correlations between the fit parameters. Again, the fits are performed largely to determine $k_{2,\mathrm{bg}}$, rather than to extrapolate k_2 to 298 K and 760 Torr. Consideration of these correlations between the fit parameters in the uncertainty analysis, as described in the ESI† for CH_2OO, indicates a median total uncertainty of 21% in the fits to $k_{2,\mathrm{obs}}$. The total uncertainties in the fits to CD_2OO decays are larger than for CH_2OO, and the fits display greater variability, since there are fewer data points for CD_2OO compared to CH_2OO, particularly at the lower pressures. Fit results and uncertainties for CD_2OO are given in Table 2.

Laser-induced fluorescence

OH(ν = 0). Fig. 5 shows a typical OH(ν = 0) time profile following the photolysis of $CH_2I_2/O_2/N_2$ mixtures. The OH(ν = 0) signal exhibited a near-instant (photolytic) production of OH(ν = 0), with a further rapid growth followed by decay. The amplitudes of the photolytic signal and of the subsequent rapid growth were both observed to display a linear dependence on the initial CH_2I_2 concentration, while the rate of the rapid growth was also observed to depend on the total pressure and on the concentration of O_2. These observations are consistent with production of OH radicals in the ground vibrational state (ν = 0) and excited vibrational states ($\nu > 0$), either directly through photolysis or through rapid reactions of species generated photolytically, followed by relaxation of the OH($\nu > 0$) to the ground vibrational state. The near-instant production of OH in ν = 0 and $\nu > 0$ states potentially occurs directly from the reaction of excited CH_2I^* with O_2, or from the rapid decomposition of excited CH_2OO^*.[38,39]

The rate of the OH(ν = 0) decay was dependent on the concentration of CH_2I_2, indicating removal of OH(ν = 0) through the expected reaction of OH with CH_2I_2. However, the observed loss of OH was not well described by a single exponential decay. Instead, it was better described by a biexponential function, indicating a slower growth of OH(ν = 0) in the system on a timescale similar to the loss through reaction with CH_2I_2. The slow growth of OH(ν = 0) in the system was attributed to production through the decomposition of CH_2OO. The production and loss of OH in the system was thus assigned to the mechanism in reactions (R1) and (R3)–(R7):

$$CH_2I_2 + h\nu \rightarrow CH_2I^* + I \quad \text{(R3)}$$

$$CH_2I^* + O_2 \rightarrow CH_2OO \quad \text{(R4)}$$

$$CH_2I^* + O_2 \rightarrow OH(\nu = 0,n) + HCO + I \quad \text{(R5)}$$

$$OH(\nu = 1) + M \rightarrow OH(\nu = 0) + M \quad \text{(R6)}$$

$$CH_2OO + M \rightarrow OH(\nu = 0,n) + \text{other products} \quad \text{(R1)}$$

$$OH(\nu = 0) + CH_2I_2 \rightarrow \text{products} \quad \text{(R7)}$$

In the reaction scheme above we assume that the relaxation of higher-lying OH vibrational states is much faster than that of OH(ν = 1) to OH(ν = 0). Reactions (R1) and (R3)–(R7) are all either first-order or occur under pseudo-first-order conditions, and thus an analytical solution can be obtained to describe the temporal behaviour of OH(ν = 0) in the system following rapid production of CH_2OO and any OH radicals resulting from photolysis (eqn (2)).

$$S_{\mathrm{OH},t} = \frac{S_{\mathrm{CH_2OO}}k_1}{(k_7' - k_1)}\left(\mathrm{e}^{-k_1 t} - \mathrm{e}^{-k_7' t}\right) + \frac{S_{\mathrm{OH}(\nu>0),t=0}k_6'}{(k_6' - k_7')}\left(\mathrm{e}^{-k_6' t} - \mathrm{e}^{-k_7' t}\right) + S_{\mathrm{OH},t=0}\mathrm{e}^{-k_7' t} \quad (2)$$

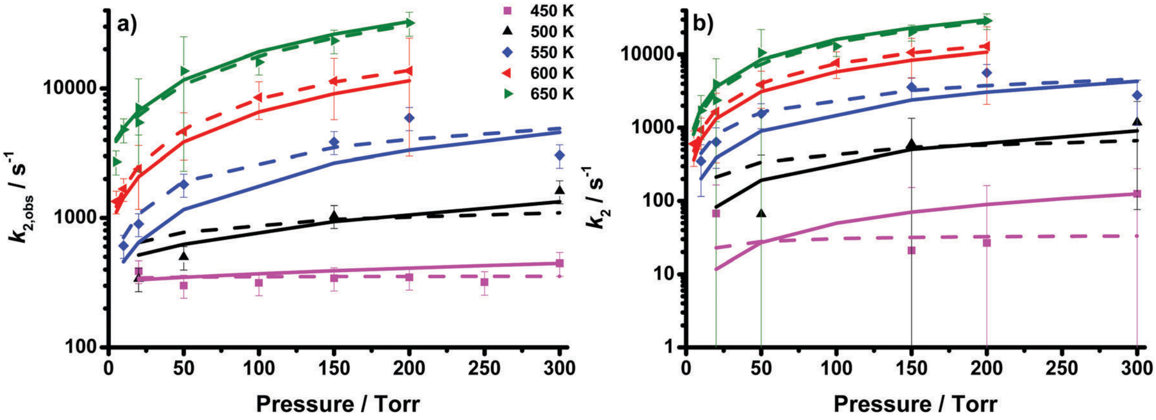

Fig. 4 Rate coefficients describing (a) the observed decay of CD_2OO ($k_{2,obs}$) and (b) the decomposition of CD_2OO ($k_2 = k_{2,obs} - k_{2,bg}$) as a function of temperature and pressure (coloured points) determined from the UV experiments. Fits to the Troe equation (dashed lines) and MESMER simulations using optimised barrier heights and $\langle\Delta E\rangle_{down}$ (solid lines) are also shown. Error bars are 1σ.

where $S_{OH,t}$ is the OH(v = 0) fluorescence signal at time t, S_{CH_2OO} is the amplitude of the OH(v = 0) signal deriving from CH_2OO decomposition, $S_{OH(v>0),t=0}$ is the amplitude of the OH(v = 0) signal deriving from vibrational relaxation of all photolytically generated OH(v > 0) states, k_1 is the rate coefficient describing the decomposition of CH_2OO, k_6' is the pseudo-first-order rate coefficient for vibrational relaxation of OH(v = 1) (*i.e.* $k_6' = k_6[M]$), and k_7' is the pseudo-first-order rate coefficient for loss of OH(v = 0), primarily through reaction with CH_2I_2 (*i.e.* $k_7' = k_7[CH_2I_2]$).

While good fits to the observed OH(v = 0) signals could be achieved, as shown in Fig. 5, the fits displayed poor sensitivity to individual rate coefficients. The complexity of the mechanism controlling OH(v = 0) in the system thus led to difficulties in obtaining reliable CH_2OO decomposition kinetics, although the temperatures and pressures over which the slow growth of OH(v = 0) in the system was apparent are consistent with those where UV absorption experiments observed CH_2OO decomposition.

The OH(v = 0) signal attributed to production from CH_2OO indicates a low yield of OH from stabilised CH_2OO decomposition. Previous experiments indicate that photolysis of CH_2I_2 at a wavelength of 248 nm leads to near-instant production of HCHO, *via* generation of excited CH_2I^* or CH_2OO^*, followed by subsequent growth of HCHO produced *via* chemistry of CH_2OO.[40,41] These experiments indicated eventual 100% yield of HCHO from CH_2OO (through reactions including CH_2OO + CH_2OO, CH_2OO + I and CH_2OO + SO_2), with the near-instant yield of HCHO representing approximately 5–10% of the total HCHO, or CH_2OO, yield. Assuming that the near-instant OH signal observed in this work is produced *via* a similar mechanism to the near-instant HCHO signal observed previously (*i.e.* *via* generation of excited CH_2I^* or CH_2OO^*), and with similar yields to the near-instant HCHO signal, we can estimate that the near-instant yield of OH also represents only 5–10% of the total CH_2OO in the system. The OH signals observed in this work were typically dominated by the near-instant signal, comprising both the instant OH(v = 0) signal and the relaxation of OH(v > 0), with the OH(v = 0) produced *via* CH_2OO decomposition being only a fraction of the total OH signal. Thus, the yields of OH(v = 0) from CH_2OO decomposition are low. For example, for the data shown in Fig. 5, the fits to eqn (2) indicate that S_{CH_2OO} is ∼(46 ± 5)% of the total OH(v = 0) signal (*i.e.* $S_{CH_2OO} + S_{OH(v=1),t=0} + S_{OH,t=0}$). If we estimate that the near-instant OH signal ($S_{OH,t=0}$ and $S_{OH(v=1),t=0}$ combined) represents only 5–10% of the total CH_2OO produced in the system, the yield of OH(v = 0) from CH_2OO decomposition is ∼4–8%. However, similarly to the kinetic analysis, a fully quantitative analysis of the OH yields in the system is not possible owing to the complexity of the mechanism and poor sensitivity of the fits to individual processes, and the data allow only a qualitative analysis of the OH yields from stabilised CH_2OO decomposition.

OH(v = 1). Measurements of OH(v = 1) data were initially performed in order to confirm assignment of the OH(v = 0) data. A typical time profile for OH(v = 1) following the photolysis of $CH_2I_2/O_2/N_2$ is shown in Fig. 6. The OH(v = 1) profile displays a near-instant growth, owing to rapid production from CH_2OO^* or CH_2I^* + O_2, as discussed for OH(v = 0), followed by growth owing to relaxation of OH(v ≥ 2) states, which are co-produced by the same process involving CH_2OO^* or CH_2I^* + O_2. The collisional relaxation of OH(v = 1) to OH(v = 0) was expected to lead to a single exponential decay for OH(v = 1). However, fits to the data indicated that the OH(v = 1) decays were more suitably described by a biexponential function which accounts for a slow growth of OH(v = 1) in the system. Fig. 6 shows the fits to the data using eqn (3). These fits were started at sufficiently long delay times (typically 100 μs), to ensure complete collisional relaxation of OH(v ≥ 2) states to OH(v = 1), since the low OH(v ≥ 2) yields made fitting the initial rise in OH(v = 1) signal difficult.[19,20]

$$S_{OH(v=1),t} = S_{OH(v=1),t=0}e^{-k_6't} + S_g e^{-k_g t} \qquad (3)$$

Here $S_{OH(v=1),t}$ is the OH(v = 1) fluorescence signal at time t, k_6' is the pseudo-first-order rate coefficient for vibrational relaxation of OH(v = 1) (*i.e.* $k_6' = k_6[M]$), and S_g is the amplitude of the signal arising from slow growth of OH(v = 1) which occurs with rate coefficient k_g.

Table 2 Decomposition kinetics of CD_2OO determined from the UV experiments. $k_{2,\mathrm{obs}}$ are the fitted CH_2OO decay rate coefficients, with 1σ listed errors. Fits to $k_{2,\mathrm{obs}}$ are derived using eqn (1), with errors given by the uncertainty analysis incorporating correlations between fit parameters as described in the ESI. $k_{2,\mathrm{Troe}}$ and $k_{2,\mathrm{bg}}$ are as defined in eqn (1). $k_{2,\mathrm{MESMER}}$ are the results of MESMER calculations. Data shown in italics were not included in the MESMER fits owing to the observed loss being dominated by the background losses. The uncertainties in $k_{2,\mathrm{MESMER}}$ are estimated from the combined uncertainties in $k_{2,\mathrm{obs}}$ and the Troe fits to $k_{2,\mathrm{obs}}$. High pressure limiting rate coefficients ($p = \infty$) are estimated from MESMER simulations up to p = 10 atm

T/K	p/Torr	$k_{2,\mathrm{obs}}$/s^{-1}	Fit to $k_{2,\mathrm{obs}}$/s^{-1}	$k_{2,\mathrm{Troe}}$/s^{-1}	$k_{2,\mathrm{bg}}$/s^{-1}	$k_{2,\mathrm{MESMER}}$/s^{-1}
450	*20*	*390 ± 10*	*345 ± 60*	*23*	*322*	*12 ± 1*
	50	*300 ± 10*	*350 ± 88*	*28*	*322*	*27 ± 3*
	100	*320 ± 10*	*353 ± 105*	*31*	*322*	*50 ± 5*
	150	*340 ± 10*	*344 ± 112*	*22*	*322*	*70 ± 7*
	200	*350 ± 10*	*354 ± 116*	*32*	*322*	*90 ± 9*
	250	*320 ± 20*	*355 ± 119*	*33*	*322*	*108 ± 12*
	300	*450 ± 20*	*355 ± 121*	*33*	*322*	*125 ± 14*
	∞					*4100 ± 3200*
500	*20*	*340 ± 20*	*645 ± 186*	*213*	*432*	*83 ± 5*
	50	500 ± 20	772 ± 343	340	432	192 ± 13
	150	1040 ± 20	975 ± 715	543	432	505 ± 38
	300	1610 ± 60	1096 ± 1056	664	432	905 ± 76
	∞					36 000 ± 25 000
550	10	610 ± 20	707 ± 200	448	259	202 ± 10
	20	900 ± 30	1075 ± 308	816	259	388 ± 17
	50	1810 ± 60	1913 ± 457	1654	259	902 ± 41
	150	3860 ± 90	3510 ± 987	3251	259	2398 ± 128
	200	5920 ± 210	4043 ± 1217	3784	259	3073 ± 172
	300	3050 ± 150	4901 ± 1593	4642	259	4329 ± 262
	∞					220 000 ± 140 000
600	5	1340 ± 10	1223 ± 139	481	742	365 ± 16
	10	1680 ± 20	1665 ± 261	923	742	693 ± 25
	20	2390 ± 1130	2528 ± 473	1786	742	1333 ± 40
	50	4650 ± 1590	4895 ± 918	4153	742	3121 ± 94
	100	8520 ± 2170	8312 ± 1314	7570	742	5844 ± 194
	150	11 420 ± 5200	11 247 ± 1576	10 505	742	8370 ± 298
	200	13 690 ± 5160	13 818 ± 1914	13 076	742	10 756 ± 406
	∞					990 000 ± 550 000
650	*5*	*2720 ± 170*	*3892 ± 114*	*811*	*3081*	*970 ± 38*
	10	4800 ± 320	4685 ± 213	1604	3081	1882 ± 59
	20	7080 ± 4600	6240 ± 380	3159	3081	3634 ± 93
	20	5460 ± 110	6240 ± 380	3159	3081	3634 ± 93
	50	13 640 ± 5510	10 733 ± 720	7652	3081	8550 ± 201
	100	15 990 ± 690	17 816 ± 996	14 735	3081	16 093 ± 382
	150	23 300 ± 1210	24 504 ± 1318	21 423	3081	23 126 ± 569
	200	31 990 ± 2024	30 864 ± 2052	27 783	3081	29 798 ± 762
	∞					3 500 000 ± 1 800 000

The kinetics of the fast component of the OH(v = 1) decay were consistent with collisional relaxation to OH(v = 0), principally by O_2,[42] and are provided in the ESI.† The kinetics of the slow component to the decay displayed a dependence on temperature and total pressure similar to that observed for CH_2OO decomposition in the UV experiments, as shown in Fig. 7. Thus, we propose that the apparent biexponential decay of OH(v = 1) results from a combination of OH(v = 1) relaxation to OH(v = 0) and direct production of OH(v = 1) from decomposition of CH_2OO. Thus, S_g in eqn (3) represents the amplitude of the OH(v = 1) signal arising from decomposition of CH_2OO and k_g is equivalent to k_1, the rate coefficient for CH_2OO decomposition. The results for k_1 determined from the OH(v = 1) experiments are summarised in Table 3 and compare well to those obtained in the UV experiments in which CH_2OO was monitored directly.

The yields of OH(v = 1) from decomposition of CH_2OO are thus low, since there is little perturbation to the OH(v = 0) signal that we attribute to OH(v = 1) relaxation. For the data shown in Fig. 6, the fitted yield of OH(v = 1) from CH_2OO decomposition is approximately 30% of the total OH(v = 1) signal. Examination of all fits for v = 0 and v = 1 OH signals leads us to conclude that if the v = 0 signal is ∼4–8% of the total CH_2OO then $v \geq 1$ is on the order of 1%.

Master equation analysis

Master equation calculations for the decomposition of CH_2OO were performed using the Master Equation Solver for Multi-Energy well Reactions (MESMER), which has been described in detail in previous work.[25,43,44] The energies of each species, including reactants, transition states and products, are divided into a number of levels, known as grains, which contain a defined number of states. These grains are assigned populations,

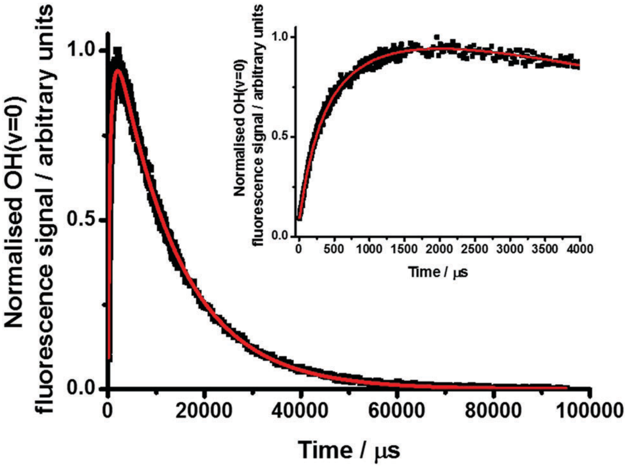

Fig. 5 Normalised OH(v = 0) LIF signal following photolysis of $CH_2I_2/O_2/N_2$ at T = 570 K and p = 20 Torr (black points) with kinetic fit (eqn (2), red line), giving k_1 = (1120 ± 30) s^{-1}. The inset shows the first 4000 µs following photolysis in greater detail.

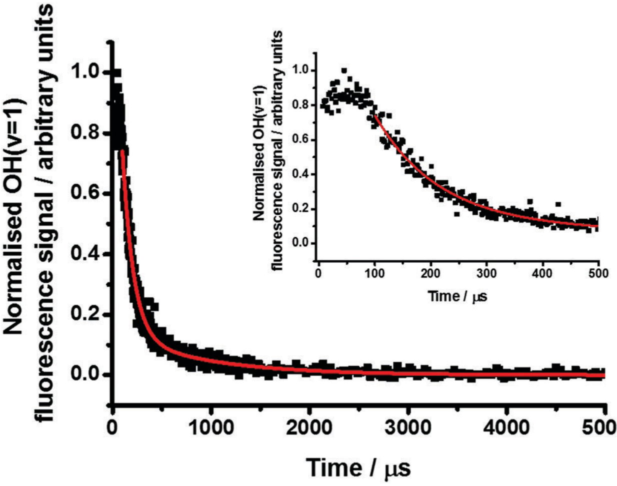

Fig. 6 Normalised OH(v = 1) LIF signal following photolysis of $CH_2I_2/O_2/N_2$ at T = 570 K and p = 20 Torr (black points) with kinetic fit (eqn (3), red line), giving k_1 = (1130 ± 30) s^{-1}. The inset shows the first 500 µs in greater detail. The fit to the data was limited to t > 100 µs after photolysis to ensure complete collisional relaxation of OH(v > 1) states.

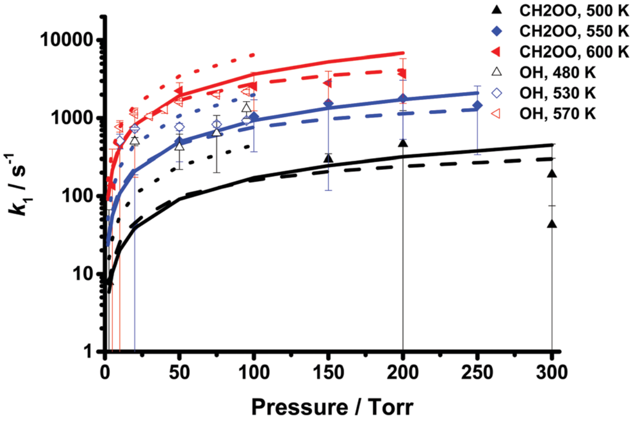

Fig. 7 Rate coefficients describing the decay of CH_2OO (k_1) as a function of temperature and pressure (coloured points) determined from the OH(v = 1) LIF experiments (open data points) and MESMER simulations using the optimised parameters from the fits to the OH data (dotted lines). Data from UV experiments monitoring CH_2OO at nearby temperatures are also shown (filled data points) alongside the corresponding Troe fits to the UV data (dashed lines) and MESMER simulations (solid lines). Error bars are 1σ.

Table 3 Decomposition kinetics of CH_2OO determined from the OH(v = 1) LIF experiments. Uncertainties in k_1 are 1σ derived from the fits to the observed OH(v = 1) profiles

T/K	p/Torr	k_1/s^{-1}
480	20	500 ± 60
	50	420 ± 200
	75	640 ± 440
	95	1310 ± 320
530	10	510 ± 110
	20	730 ± 30
	50	770 ± 80
	75	830 ± 70
	95	930 ± 70
570	10	770 ± 110
	20	1130 ± 30
	30	1060 ± 80
	40	1300 ± 150
	50	1600 ± 60
	75	2000 ± 100
	95	2190 ± 140

average energies, and, where appropriate, average values of microcanonical rate coefficients, forming the basis for the master equation analysis. Changes in the population distribution among the grains occur through collisional energy transfer *via* interactions with a thermal bath gas or *via* transfer from one species to another *via* reactions governed by the microcanonical rate coefficients in the system.

The equation of motion of the grain population probabilities is represented by:

$$\mathrm{d}\mathbf{p}/\mathrm{d}t = \mathbf{M}\mathbf{p} \qquad (4)$$

where **p** is a vector containing the populations of the energy grains and **M** is a matrix that contains transition rates between grains and determines the evolution of the grain population distribution owing to collisional activation/deactivation or reaction. The reactive processes are described by Rice, Ramsperger, Kassel and Marcus (RRKM) theory, with a temperature-dependent exponential down model (eqn (5)) used to describe collisional transfer energy:

$$\langle\Delta E\rangle_{\mathrm{down},T} = \langle\Delta E\rangle_{\mathrm{down,298K}}(T/298)^n \qquad (5)$$

where $\langle\Delta E\rangle_{\mathrm{down},T}$ represents the average energy transferred in a downward direction on collision with the bath gas at temperature T, and n is the exponent used to parameterise the temperature dependence.

For the master equation calculations presented in this work, geometries, frequencies and rotational constants for CH_2OO, transition states to decomposition and the decomposition products were provided by the calculations of Nguyen *et al.*[11] at the CCSD(T)/aug-cc-pVTZ//B3LYP/aug-cc-pVTZ level of theory, with the roaming channel leading to formic acid excluded, as suggested by recent improved calculations.[12] If the roaming channel were active, a strong kinetic isotope effect might be expected between CH_2OO and CD_2OO, which is not supported by the experimental data or the calculations reported in this work. Geometries, frequencies and rotational constants for CD_2OO, the transition state to decomposition and the initial intermediate leading to decomposition products were calculated using the Gaussian 09 suite of programs[45] at the M06-2X/aug-cc-pVTZ[46–51] level of theory. The barrier to decomposition was improved *via* single point energy computations (SPE) of the stationary structures using coupled cluster calculations with single, double and perturbative triple excitations (CCSD(T)).[52] The SPEs were extrapolated to the complete basis set limit (CBS) with the use of correlation-consistent basis sets (aug-cc-pVXT, X = D, T, Q)[47–51] and the extrapolation scheme presented by Peterson *et al.*[48] Barrier heights and stationary point energies were corrected for zero point energies (ZPEs), and although the deuterated reactant does have a lower ZPE compared to the non-deuterated reactant, the same effect is observed in the respective transition states, such that the barrier height is similar between the deuterated and non-deuterated systems. The barrier calculated at the CCSD(T)/CBS//M06-2//aug-cc-pVTZ level of theory (81.04 kJ mol^{-1}) is in agreement with the barrier of 78.24 kJ mol^{-1} obtained by Nguyen *et al.*[11] for CH_2OO.

Pressure dependent rate coefficients for CH_2OO and CD_2OO were calculated by MESMER using an inverse Laplace transformation to determine microcanonical rate coefficients ($k(E)$), with molecular densities of states calculated by a rigid rotor-harmonic oscillator approximation.[43] A grain size of 100 cm^{-1} was used in the calculations described here. The molecular constants and further details regarding the calculations are given in the ESI.†

The master equation calculations were optimised by varying the parameters $\langle \Delta E \rangle_{\text{down,298K}}$ and n in eqn (5), as well as the barrier height to decomposition. A fit to the rate coefficients for CH_2OO and CD_2OO determined from the UV experiments, was performed using a Levenburg–Marquardt algorithm to minimise the merit function χ^2, as defined by eqn (6):

$$\chi^2 = \sum_{i=1}^{N} \frac{\left(k_{\text{exp}}(T_i, p_i) - k_{\text{model}}(T_i, p_i)\right)^2}{\sigma_i^2} \tag{6}$$

where $k_{\text{exp}}(T_i,p_i)$ and $k_{\text{model}}(T_i,p_i)$ are the experimental and modelled rate coefficients at temperature T_i and pressure p_i, respectively, σ_i^2 is the experimental uncertainty at temperature T_i and pressure p_i, N is the total number of experimental measurements, and $k_{\text{exp}}(T_i,p_i)$ is the experimentally determined value of k_1 (or k_2) after subtraction of $k_{1,\text{bg}}$ (or $k_{2,\text{bg}}$). The temperatures and pressures used in the fits to eqn (5) for CH_2OO and CD_2OO are highlighted in Tables 1 and 2, respectively. In both cases, only data at temperatures which show a clear pressure dependence and which have a positive value for k_1 or k_2 after the subtraction of $k_{1,\text{bg}}$ or $k_{2,\text{bg}}$ from $k_{1,\text{obs}}$ or $k_{2,\text{obs}}$, respectively, are included in the fits. Thus, data at temperatures below 500 K are excluded from the fits, and some of the data at low pressures are excluded owing to the uncertainties in separating the decomposition from the background loss when the decomposition is slow compared to the background losses resulting from reaction with the precursor and diffusion.

Since the decomposition of CH_2OO is thought to proceed *via* a single barrier,[11,12,14,23] optimisation of $\langle \Delta E \rangle_{\text{down,298K}}$, n and the barrier to decomposition can be achieved through consideration of the simplified potential energy surface shown in blue in Fig. 8, consisting of only CH_2OO, the first transition state (TS2), and the cyclic intermediate (dioxirane). An analogous PES was used for CD_2OO, in which a further simplification

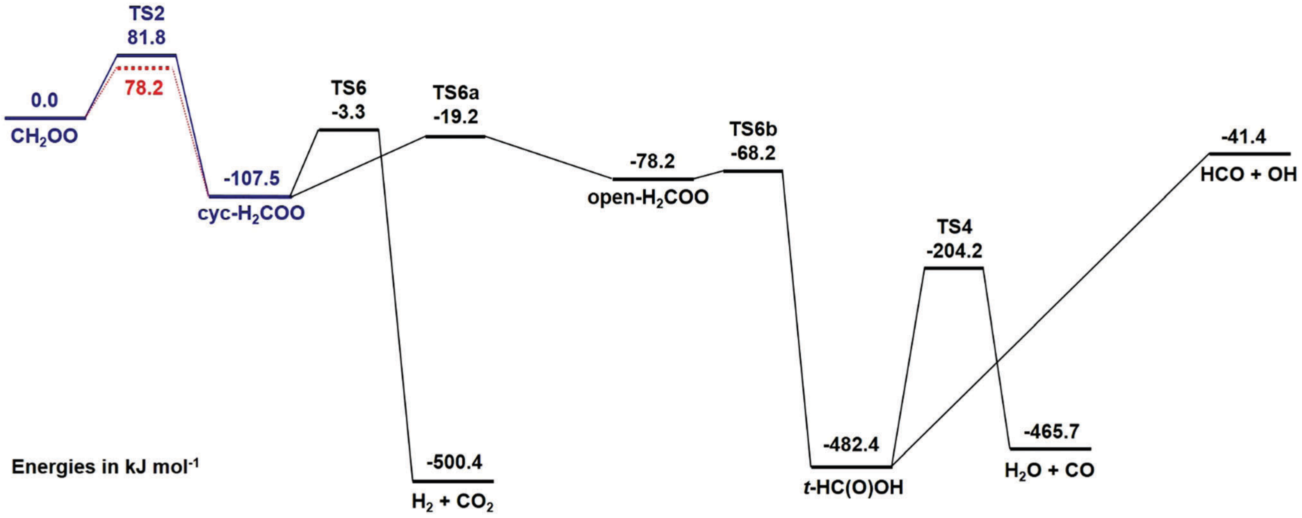

Fig. 8 Potential energy surface for CH_2OO decomposition, showing the optimised barrier to decomposition (blue) and the calculated barrier (red).[11] The simplified potential energy surface used to optimise the MESMER simulations is shown in blue (*i.e.* comprising CH_2OO, TS2 and the intermediate cyc-H_2COO (dioxirane)), with the full PES used to estimate product yields shown in black. Names of transition states and intermediates are analogous to those reported by Nguyen *et al.*[11]

Table 4 Optimised parameters describing the decomposition of CH_2OO and CD_2OO obtained from the master equation fits to the observed decomposition kinetics. Uncertainties are 1σ obtained from the MESMER fits. Optimised parameters obtained from observations of OH are not included owing to significant uncertainties in the kinetic fits

	Barrier to decomposition/kJ mol^{-1}	$\langle\Delta E\rangle_{down}/cm^{-1}$	$k_{(T=298K, p=760\,Torr)}/10^{-3}\ s^{-1}$
CH_2OO	81.8 ± 6.2	$(32.6 \pm 13.7)(T/298\ K)^{(1.7\pm0.4)}$	$1.1^{+1.5}_{-1.1}$
CD_2OO	80.1 ± 3.0	$(39.6 \pm 7.8)(T/298\ K)^{(1.3\pm0.2)}$	$5.5^{+9.2}_{-5.5}$

was made such that it considers only the energies of CD_2OO and the initial transition state which ultimately leads to product formation.

Fig. 8 shows the results of the optimisation of the barrier to decomposition of CH_2OO, with the comparison between the experimentally observed rate coefficients for CH_2OO decomposition and the output from the MESMER optimisation given in Fig. 2 and Table 1. The MESMER fits to the data yield $\langle\Delta E\rangle_{down}$ = $(32.6 \pm 13.7)(T/298\ K)^{(1.7\pm0.4)}$ cm^{-1}, and require an increase of 3.6 kJ mol^{-1} in the calculated barrier height from 78.2 kJ mol^{-1} to 81.8 kJ mol^{-1}, giving $k_1 = 1.1^{+1.5}_{-1.1} \times 10^{-3}\ s^{-1}$ in He at T = 298 K and p = 760 Torr. For the experimental conditions surveyed in this work, the value for $\langle\Delta E\rangle_{down}$ ranges from 65 cm^{-1} at T = 450 K to 121 cm^{-1} at T = 650 K. The optimised parameters are given in Table 4. Although the increase in the barrier height is greater than the estimated uncertainty of $\sim$2 kJ mol^{-1} in calculations of this nature,[7] the optimised barrier in MESMER is also subject to uncertainties of several kJ mol^{-1}, and the calculations may be influenced by multireference effects which could result in additional uncertainty. Optimisation of $\langle\Delta E\rangle_{down}$ in N_2 was also performed using the data obtained from measurements of OH (shown in Table 3) with the barrier to decomposition constrained to the value of 81.8 kJ mol^{-1} as indicated by the UV experiments. Fig. 7 shows the results of the optimisation, which gave $\langle\Delta E\rangle_{down}$ = $(125.4 \pm 32.2)(T/298\ K)^{(0.5\pm0.4)}$ cm^{-1} and k_1 = 0.01 s^{-1} at 298 K and 760 Torr in N_2. Uncertainties in the value of k_1 in N_2 at 298 K and 760 Torr determined from the OH experiments, determined by propagation of errors in the MESMER fits, are on the order of $\sim$200%. However, as shown in Fig. 7 the optimisation tends to overpredict the observed rate coefficients, and the results may be subject to larger uncertainties than indicated by the statistical error propagation owing to the complexity of the mechanism controlling the production and loss of OH in the system.

The results of Berndt *et al.*[23] required a decrease in the calculated barrier height from 78.9 kJ mol^{-1} to 76.8 kJ mol^{-1} to improve the agreement between the master equation calculation and the measured rate coefficient for decomposition of $(0.19 \pm 0.07)\ s^{-1}$ at 298 K and 760 Torr in N_2 using the free-jet flow reactor. The higher barrier height determined in this work from the UV observations of CH_2OO in He lead to a lower value of $k_1 = 1.1 \times 10^{-3}\ s^{-1}$ at 298 K and 760 Torr compared to the work of Berndt *et al.*[23] The difference in the barrier heights is significant, but it is worth noting that the barrier height determined by Berndt *et al.* was fitted to a single measurement of k_1, while that determined in this work fitted over a range of temperatures and pressures, providing greater constraint in the fit to eqn (6). The experiments reported in this work also use direct detection of CH_2OO, while the experiments of Berndt *et al.* rely on titration of CH_2OO to H_2SO_4, with subsequent ionisation and detection of H_2SO_4.

Simulations in MESMER using the full PES by Nguyen *et al.*,[11] shown in Fig. 8, with the optimised values for $\langle\Delta E\rangle_{down}$ and TS2 energy, determined from the UV experiments, were performed at p = 1–3040 Torr and T = 400–1200 K to investigate the product distribution. There was little variation in the product distribution over the pressure and temperature ranges investigated, with yields of 63.7% for $H_2 + CO_2$ and 36.0% for $H_2O + CO$, on average. The yields of OH + HCO is predicted to be 0.3%, on average, and is lower than the estimates based on the OH measurements reported in this work and those indicated by the use of OH as a proxy to CH_2OO in experiments by Liu *et al.*[16] and Li *et al.*[17]

The optimised TS2 energy and $\langle\Delta E\rangle_{down}$ were also used in MESMER simulations to calculate k_1 at temperatures between 200 K and 850 K and pressures up to 10 atm. The calculated rate coefficients were subsequently parameterised using the Troe expression for broad falloff curves[53] (eqn (7)–(9)) for use in kinetic models:

$$k = \frac{k_0[\mathrm{M}]k_\infty}{k_0[\mathrm{M}] + k_\infty}F \tag{7}$$

$$F = \frac{(1 + k_0[\mathrm{M}]/k_\infty)}{(1 + (k_0[\mathrm{M}]/k_\infty)^n)^{1/n}} \tag{8}$$

$$\begin{aligned} n &= \left(\frac{\ln(2)}{\ln(2/F_c)}\right)(0.8 + 0.2(k_0[\mathrm{M}]/k_\infty)^q) \\ q &= \frac{(F_c - 1)}{\ln(F_c/10)} \end{aligned} \tag{9}$$

where $k_{1,0}(T)$ is the low-pressure and $k_{1,\infty}(T)$ is the high-pressure limiting rate coefficient for CH_2OO decomposition, M is the total number density, and F_c is the broadening factor. The fits to the MESMER output for k_1 give $k_{1,0}$ = $3.2 \times 10^{-4}(T/298)^{-5.81}\exp(-12\,770/T)$ $cm^3\ s^{-1}$, $k_{1,\infty} = 1.4 \times 10^{13}(T/298)^{0.06}\exp(-10\,010/T)\ s^{-1}$ and F_c = 0.447.

Analogous results for CD_2OO give $\langle\Delta E\rangle_{down}$ = $(39.6 \pm 7.8)(T/298\ K)^{(1.3\pm0.2)}$ cm^{-1} and a barrier to decomposition of 80.1 kJ mol^{-1}, a decrease of 0.9 kJ mol^{-1} from the calculated barrier of 81.0 kJ mol^{-1}, with $\langle\Delta E\rangle_{down}$ thus ranging from 67 cm^{-1} at 450 K to 109 cm^{-1} at 650 K. The fits give a value of $k_2 = 5.5^{+9.2}_{-5.5} \times 10^{-3}\ s^{-1}$ in He at T = 298 K and p = 760 Torr. The comparison between the experimentally observed rate coefficients and the MESMER output is given in Fig. 4 and Table 2, with the optimised parameters summarised in Table 4.

Fits to eqn (7)–(9), using the optimised parameters for CD_2OO in MESMER to calculate k_2 at temperatures between 200 K and 850 K and pressures up to 10 atm, give $k_{2,0} = 5.2 \times 10^{-5}(T/298)^{-5.28}\exp(-11\,610/T)$ $cm^3\ s^{-1}$, $k_{2,\infty} = 1.2 \times 10^{13}(T/298)^{0.06}\exp(-9800/T)\ s^{-1}$ and $F_c = 0.427$.

The optimised PES thus indicates that there is no significant change in the barrier height to decomposition upon deuteration of CH_2OO. However, comparison of Fig. 2 and 4 shows that CD_2OO decomposes faster than CH_2OO under equivalent conditions, which is also confirmed by the MESMER calculations. Given the similar electronic barriers to decomposition for CH_2OO and CD_2OO, such differences likely result from an increased density of states in CD_2OO near the transition state, which promotes the high pressure limit at lower pressures. A similar effect has been observed in a recent study of deuterated Criegee intermediate kinetics, in the reactions of $(CH_3)_3COO$ and $(CD_3)_3COO$ with SO_2,[54] and was attributed to the potential impact of increased collisional stabilisation of the deuterated association complex between $(CD_3)_3COO$ and SO_2 compared to $(CH_3)_3COO$ and SO_2 owing to the increased density of vibrational states in the deuterated system.

Conclusions

The decomposition kinetics of CH_2OO Criegee intermediate have been investigated at temperatures between 450 K and 650 K and pressures in the range 2–350 Torr of He using flash photolysis of CH_2I_2 in O_2 and a combination of time-resolved cavity enhanced broadband UV absorption spectroscopy, for direct monitoring of CH_2OO, and laser-induced fluorescence, for monitoring of OH decomposition products. Kinetics of CD_2OO decomposition were also investigated using flash photolysis of CD_2I_2 with time-resolved cavity enhanced broadband UV absorption spectroscopy.

The decomposition of CH_2OO is expected to be slow under ambient conditions, and thus is not a significant sink for CH_2OO in the atmosphere or in chamber experiments of ozonolysis reactions, despite reports in previous work. Master equation fits using MESMER give $k_1 = 1.1^{+1.5}_{-1.1} \times 10^{-3}\ s^{-1}$ at 298 K and 760 Torr in He, using an exponential down model to describe the collisional energy transfer, where $\langle \Delta E \rangle_{down} = (32.6 \pm 13.7)(T/298\ K)^{(1.7\pm0.4)}\ cm^{-1}$, and requiring an increase in the calculated barrier height to decomposition from 78.2 $kJ\ mol^{-1}$ to 81.8 $kJ\ mol^{-1}$. Product yields, determined from MESMER simulations using the increased barrier height to decomposition, are predicted to be 63.7% for $H_2 + CO_2$, 36.0% for $H_2O + CO$ and 0.3% for OH + HCO. For CD_2OO, the master equation fits give $k_2 = 5.5^{+9.2}_{-5.5} \times 10^{-3}\ s^{-1}$ at 298 K and 760 Torr in He, and give values of $\langle \Delta E \rangle_{down} = (39.6 \pm 7.8)(T/298\ K)^{(1.3\pm0.2)}\ cm^{-1}$ and a barrier height of 80.1 $kJ\ mol^{-1}$ compared to the calculated value of 81.0 $kJ\ mol^{-1}$. We observed no kinetic isotope effect between the decomposition kinetics of CH_2OO and CD_2OO.

Results from this work provide a detailed description of CH_2OO decomposition kinetics that can be applied to the analysis of the decomposition and stabilisation of nascent CH_2OO Criegee intermediates produced in ozonolysis reactions, and to assess the contributions of wall losses to larger SCI species produced by ozonolysis in chamber experiments, which decompose more rapidly under ambient conditions owing to the existence of alternative decomposition pathways. Measurements reporting combined kinetics of CH_2OO decomposition and wall loss are likely dominated by wall losses,[19–22] and can therefore provide an estimate for SCI wall loss rates that could be applied to other SCI species, enabling separation of the wall loss rate and decomposition rate in chamber experiments.

The low yield of OH radicals observed indicates that decomposition of CH_2OO cannot be responsible for any potential OH interferences in field instruments measuring ambient OH concentrations using the LIF-FAGE (laser-induced fluorescence with fluorescence assay by gas expansion) technique, as has been postulated in the literature.[18] Under combustion conditions, decomposition of CH_2OO will be rapid, with a fraction of decomposition leading to production of OH and HCO radicals, and thus contributing to chain-branching processes. The role of CH_2OO in combustion, however, has yet to be fully established.

Conflicts of interest

There are no conflicts to declare.

Acknowledgements

We would like to thank T.-N. Nguyen, R. Putikam and M. C. Lin for providing details of their calculations on the potential energy surface for CH_2OO decomposition. DS would like to thank the Natural Environment Research Council (NERC) for the award of an Independent Research Fellowship (grant reference NE/L010798/1) and New Investigator grant (grant reference NE/P012876/1) for funding. This material is based upon work supported by the Division of Chemical Sciences, Geosciences and Biosciences, Office of Basic Energy Sciences (BES), U.S. Department of Energy (USDOE). Sandia National Laboratories is a multimission laboratory managed and operated by National Technology and Engineering Solutions of Sandia, LLC., a wholly owned subsidiary of Honeywell International, Inc., for the USDOE's National Nuclear Security Administration under contract DE-NA0003525. This paper describes objective technical results and analysis. Any subjective views or opinions that might be expressed in the paper do not necessarily represent the views of the USDOE or the United States Government. LS was supported by the Division of Chemical Sciences, Geosciences and Biosciences, BES/USDOE, through the Argonne-Sandia Consortium on High Pressure Combustion Chemistry. ZD was supported by the DOE Office of Science Workforce Development Program for Teachers and Scientists Summer Undergraduate Laboratory Internship. DJM would like to thank the Brazilian National Council for Scientific and Technological Development (CNPq, grant reference 206527/2014-4).

References

1 D. Johnson and G. Marston, *Chem. Soc. Rev.*, 2008, **37**, 699.

2 T. B. Nguyen, G. S. Tyndall, J. D. Crounse, A. P. Teng, K. H. Bates, R. H. Schwantes, M. M. Coggon, L. Zhang, P. Feiner, D. O. Milller, K. M. Skog, J. C. Rivera-Rios, M. Dorris, K. F. Olson, A. Koss, R. J. Wild, S. S. Brown, A. H. Goldstein, J. A. de Gouw, W. H. Brune, F. N. Keutsch, J. H. Seinfeldcj and P. O. Wennberg, *Phys. Chem. Chem. Phys.*, 2016, **18**, 10241.

3 D. L. Osborn and C. A. Taatjes, *Int. Rev. Phys. Chem.*, 2015, **34**, 309.

4 C. A. Taatjes, D. E. Shallcross and C. J. Percival, *Phys. Chem. Chem. Phys.*, 2014, **16**, 1704.

5 M. C. Smith, W. Chao, K. Takahashi, K. A. Boering, J. J.-M. Lin and J. Jr-Min, *J. Phys. Chem. A*, 2016, **120**, 4789–4798.

6 N. M. Kidwell, H. Li, X. Wang, J. M. Bowman and M. I. Lester, *Nat. Chem.*, 2016, **8**, 509.

7 Y. Fang, F. Liu, V. P. Barber, S. J. Klippenstein, A. B. McCoy and M. I. Lester, *J. Chem. Phys.*, 2016, 144.

8 Y. Fang, F. Liu, S. J. Klippenstein and M. I. Lester, *J. Chem. Phys.*, 2016, **145**, 044312.

9 A. Andersen and E. A. Carter, *J. Phys. Chem. A*, 2003, **107**, 9463.

10 A. Andersen and E. A. Carter, *Mol. Phys.*, 2008, **106**, 367.

11 T.-N. Nguyen, R. Putikam and M. C. Lin, *J. Chem. Phys.*, 2015, 142.

12 L. B. Harding and S. J. Klippenstein, *J. Chem. Phys.*, 2015, 143.

13 C. F. Goldsmith, L. B. Harding, Y. Georgievskii, J. A. Miller and S. J. Klippenstein, *J. Phys. Chem. A*, 2015, **119**, 7766.

14 T. L. Nguyen, H. Lee, D. A. Matthews, M. C. McCarthy and J. F. Stanton, *J. Phys. Chem. A*, 2015, **119**, 5524.

15 M. Pfeifle, Y.-T. Ma, A. W. Jasper, L. B. Harding, W. L. Hase and S. J. Klippenstein, *J. Chem. Phys.*, 2018, **148**, 174306.

16 Y. Liu, K. D. Bayes and S. P. Sander, *J. Phys. Chem. A*, 2014, **118**, 741.

17 Y. Q. Liu, F. H. Liu, S. Y. Liu, D. X. Dai, W. R. Dong and X. M. Yang, *Phys. Chem. Chem. Phys.*, 2017, **19**, 20786.

18 A. Novelli, L. Vereecken, J. Lelieveld and H. Harder, *Phys. Chem. Chem. Phys.*, 2014, **16**, 19941.

19 M. J. Newland, A. R. Rickard, M. S. Alam, L. Vereecken, A. Munoz, M. Rodenas and W. J. Bloss, *Phys. Chem. Chem. Phys.*, 2015, **17**, 4076.

20 M. J. Newland, A. R. Rickard, L. Vereecken, A. Munoz, M. Rodenas and W. J. Bloss, *Atmos. Chem. Phys.*, 2015, **15**, 9521.

21 R. Chhantyal-Pun, A. Davey, D. E. Shallcross, C. J. Percival and A. J. Orr-Ewing, *Phys. Chem. Chem. Phys.*, 2015, **17**, 3617.

22 T. Berndt, J. Voigtlander, F. Stratmann, H. Junninen, R. L. Mauldin, M. Sipila, M. Kulmala and H. Herrmann, *Phys. Chem. Chem. Phys.*, 2014, **16**, 19130.

23 T. Berndt, R. Kaethner, J. Voigtlander, F. Stratmann, M. Pfeifle, P. Reichle, M. Sipila, M. Kulmala and M. Olzmann, *Phys. Chem. Chem. Phys.*, 2015, **17**, 19862.

24 M. Olzmann, E. Kraka, D. Cremer, R. Gutbrod and S. Andersson, *J. Phys. Chem. A*, 1997, **101**, 9421.

25 D. R. Glowacki, C.-H. Liang, C. Morley, M. J. Pilling and S. H. Robertson, *J. Phys. Chem. A*, 2012, **116**, 9545.

26 L. Sheps, *J. Phys. Chem. Lett.*, 2013, **4**, 4201.

27 L. Sheps, A. M. Scully and K. Au, *Phys. Chem. Chem. Phys.*, 2014, **16**, 26701.

28 Z. C. J. Decker, K. Au, L. Vereecken and L. Sheps, *Phys. Chem. Chem. Phys.*, 2017, **19**, 8541.

29 D. R. Glowacki, J. Lockhart, M. A. Blitz, S. J. Klippenstein, M. J. Pilling, S. H. Robertson and P. W. Seakins, *Science*, 2012, **337**, 1066.

30 S. A. Carr, M. T. B. Romero, M. Blitz, M. J. Pilling, D. E. Heard and P. W. Seakins, *Chem. Phys. Lett.*, 2007, 108.

31 M. T. Baeza-Romero, D. R. Glowacki, M. A. Blitz, D. E. Heard, M. J. Pilling, A. R. Rickard and P. W. Seakins, *Phys. Chem. Chem. Phys.*, 2007, **9**, 4114.

32 J. Troe, *J. Phys. Chem.*, 1979, **83**, 114.

33 J. B. Burkholder, S. P. Sander, J. Abbatt, J. B. Barker, R. E. Huie, C. E. Kolb, M. J. Kurylo, V. L. Orkin, D. M. Wilmouth and P. H. Wine, JPL Publication 15-10 2015, Jet Propulsion Laboratory, http://jpldataeval.jpl.nasa.gov.

34 R. Atkinson, D. L. Baulch, R. A. Cox, J. N. Crowley, R. F. Hampson, R. G. Hynes, M. E. Jenkin, M. J. Rossi and J. Troe, *Atmos. Chem. Phys.*, 2004, **4**, 1461.

35 A. W. L. Ting and J. J. M. Lin, *J. Chin. Chem. Soc.*, 2017, **64**, 360.

36 W.-L. Ting, Y.-H. Chen, W. Chao, M. C. Smith and J. J.-M. Lin, *Phys. Chem. Chem. Phys.*, 2014, **16**, 10438.

37 E. S. Foreman, K. M. Kapnas, Y. Jou, J. Kalinowski, D. Feng, R. B. Gerber and C. Murray, *Phys. Chem. Chem. Phys.*, 2015, **17**, 32539.

38 J. H. Lehman, H. W. Li and M. I. Lester, *Chem. Phys. Lett.*, 2013, **590**, 16.

39 J. H. Lehman, H. W. Li, J. M. Beames and M. I. Lester, *J. Chem. Phys.*, 2013, 139.

40 D. Stone, M. Blitz, L. Daubney, T. Ingham and P. Seakins, *Phys. Chem. Chem. Phys.*, 2013, **15**, 19119.

41 D. Stone, M. Blitz, L. Daubney, N. U. M. Howes and P. Seakins, *Phys. Chem. Chem. Phys.*, 2014, **16**, 1139.

42 D. C. McCabe, I. W. M. Smith, B. Rajakumar and A. R. Ravishankara, *Chem. Phys. Lett.*, 2006, **421**, 111.

43 R. J. Shannon, A. S. Tomlin, S. H. Robertson, M. A. Blitz, M. J. Pilling and P. W. Seakins, *J. Phys. Chem. A*, 2015, **119**, 7430.

44 K. W. McKee, M. A. Blitz, P. A. Cleary, D. R. Glowacki, M. J. Pilling, P. W. Seakins and L. M. Wang, *J. Phys. Chem. A*, 2007, **111**, 4043.

45 M. J. Frisch, *et al.*, *Gaussian 09, Revision D.01*, Gaussian Inc., Wallingford, CT, 2009.

46 Y. Zhao and D. G. Truhlar, *Theor. Chem. Acc.*, 2008, **120**, 215.

47 A. K. Wilson, T. van Mourik and T. H. Dunning, *J. Mol. Struct.*, 1996, **388**, 339.

48 K. A. Peterson, D. E. Woon and T. H. Dunning, *J. Chem. Phys.*, 1994, **100**, 7410.

49 R. A. Kendall, T. H. Dunning and R. J. Harrison, *J. Chem. Phys.*, 1992, **96**, 6796.

50 T. H. Dunning, *J. Chem. Phys.*, 1989, **90**, 1007.

51 D. E. Woon and T. H. Dunning, *J. Chem. Phys.*, 1993, **98**, 1358.

52 K. Raghavachari, G. W. Trucks, J. A. Pople and M. Headgordon, *Chem. Phys. Lett.*, 1989, **157**, 479.

53 J. Troe and V. G. Ushakov, *Z. Phys. Chem.*, 2014, **228**, 1.

54 R. Chhantyal-Pun, O. Welz, J. D. Savee, A. J. Eskola, E. P. F. Lee, L. Blacker, H. R. Hill, M. Ashcroft, M. A. H. Khan, G. C. Lloyd-Jones, L. Evans, B. Rotavera, H. F. Huang, D. L. Osborn, D. K. W. Mok, J. M. Dyke, D. E. Shallcross, C. J. Percival, A. J. Orr-Ewing and C. A. Taatjes, *J. Phys. Chem. A*, 2017, **121**, 4.